Three-dimensional total internal reflection fluorescence nanoscopy with sub-10 nm resolution

Alan M. Szalai[1‡], Bruno Siarry[1‡], Jerónimo Lukin[2], David J. Williamson[3], Nicolás Unsain[4], Raquel Becerra[2], Damián Refojo[2], Alfredo Cáceres[4,5], Mauricio Pilo-Pais[6], Guillermo Acuna[6], Dylan M. Owen [3,7], Sabrina Simoncelli[3*] and Fernando D. Stefani[1,8*]

[1]Centro de Investigaciones en Bionanociencias (CIBION), Consejo Nacional de Investigaciones Científicas y Técnicas (CONICET), Godoy Cruz 2390, C1425FQD Ciudad Autónoma de Buenos Aires, Argentina

[2]Instituto de Investigación en Biomedicina de Buenos Aires (IBioBA)-CONICET-Partner Institute of the Max Planck Society, Godoy Cruz 2390, C1425FQD Ciudad Autónoma de Buenos Aires, Argentina

[3]Department of Physics and Randall Centre for Cell and Molecular Biophysics, King's College London, London, UK

[4]Instituto Investigación Médica Merecedes y Martín Ferreyra-INIMEC-CONICET-Universidad Nacional Córdoba, Friuli 2434 X5016NST Córdoba, Argentina

[5]Instituto Universitario Ciencias Biomédicas de Córdoba (IUCBC), Friuli 2786, X5016NSW Córdoba, Argentina

[6]Department of Physics, University of Fribourg, Chemin du Musée 3, Fribourg CH-1700, Switzerland

[7]Institute of Immunology and Immunotherapy, Department of Mathematics and Centre for Membrane Proteins and Receptors, University of Birmingham, Birmingham, UK

[8]Departamento de Física, Facultad de Ciencias Exactas y Naturales, Universidad de Buenos Aires, Güiraldes 2620, C1428EHA Ciudad Autónoma de Buenos Aires, Argentina

‡These authors contributed equally to this work

Here, we present a single-molecule localization microscopy (SMLM) analysis method that delivers sub-10 nm *z*-resolution when combined with 2D total internal reflection (TIR) fluorescence imaging via DNA point accumulation for imaging nanoscale topography (DNA-PAINT). Axial resolution is obtained from a precise measurement of the emission intensity of single molecules under evanescent field excitation. This method can be implemented on any conventional TIR wide-field microscope without modifications. We validate this approach by resolving the periodicity of alpha-tubulin assembly in microtubules, demonstrating isotropic resolution below 8 nm.

Main

Imaging the three-dimensional organization of biological structures down to the size of their structural proteins, ~ 4 to 10 nm, can open up exciting opportunities in the life sciences. Recently, two techniques outstand for reaching this level of resolution in two-dimensions: DNA-PAINT[1,2] and MINFLUX[3]. Although both methods provide lateral resolutions well below 10 nm, the issue is not yet solved for the axial counterpart. Axial resolution of fluorescence nanoscopy using a single objective lens lies in the range of 35 to 120 nm for both coordinate-targeted and coordinate-stochastic methods[4,5], including recent intensity-based approaches that rely on supercritical angle fluorescence or accurate photometry determination[6,7]. By exploiting the 4Pi configuration[8] it is possible to reach axial resolution below 35 nm, but at the cost of increased technical complexity. Isotropic STED (isoSTED) has been shown to deliver nearly isotropic resolution in the range of 30 to 40 nm[9,10], whereas 4-Pi PALM/STORM has reached 10 to 20 nm resolution in 3D[11–13]. To date, sub-10 nm axial resolution was only achieved by decoding *z*-position of fluorophores through lifetime imaging making use of the distance-dependent energy transfer from excited fluorophores to a metal film[14] or a graphene sheet[15]. However, combining these ns time-resolved methods with other nanoscopy methods in order to obtain 3D imaging with sub-10 nm resolution is not straightforward[16].

Here, we present Supercritical Illumination Microscopy by Photometric *z*-Localization Encoding (SIMPLE), an easy-to-implement photometric method to determine the axial position

of molecules near a dielectric interface under total internal reflection excitation. Under this condition, fluorescent molecules that are closer to the interface appear brighter due to two factors. First, they are excited more efficiently because the TIR illumination field decays exponentially from the interface. Second, molecules closer to the interface emit more photons into the glass semi-space and into the collection solid angle. SIMPLE consists of calibrating the detected fluorescence signal considering these two effects in order to retrieve the axial position of single molecules from a direct measurement of their detected fluorescence intensity. SIMPLE can be combined with any fluorescence nanoscopy method based on localization of single molecules. In combination with DNA-PAINT, SIMPLE delivers sub-10 nm resolution in all three dimensions, enabling the direct recognition of protein assemblies at the molecular level.

Figure 1 illustrates the concept of SIMPLE. TIR occurs when light incides from a medium with refractive index n_i on an interface with another medium of smaller refractive index $n_s < n_i$. If the angle of incidence θ_i is larger than the critical angle $\theta_C = \arcsin(n_s/n_i)$, light is fully reflected at the interface and an evanescent field appears, penetrating the medium of low refractive index with an intensity that decays exponentially. In a fluorescence microscope, TIR illumination can be generated by controlling the angle of incidence of the excitation light using an immersion objective lens as schematically shown in the inset of Figure 1a. In practice, the excitation field contains also a non-evanescent component due to scattering, that decays on a much longer scale[17]. Near the interface, the non-evanescent component can be considered constant and the overall illumination field is represented by a linear superposition of both contributions, $I(z) = \alpha I_0 e^{-z/d} + (1 - \alpha)I_0$ with I_0 the intensity at the interface, $d = \lambda_0/4\pi/(n_i^2\sin^2(\theta_i) - n_s^2)^{-1/2}$ the penetration depth, λ_0 the vacuum wavelength, and $1 - \alpha$ the scattering contribution fraction. Figure 1a shows $I(z)$ for our configuration ($\lambda_0 = 642$ nm, $n_i = 1.517, n_s = 1.33$ water, $\theta_i = 69.5°, \alpha = 0.9$), which decays with $d = 102$ nm. The excitation rate of a fluorophore (under linear excitation) will depend on the axial position according to $I(z)$. The fraction of the fluorescence emission collected by the solid angle of the microscope objective also depends on the axial position of the fluorophore, as well as on the relative orientation of its emission dipole to the interface[18]. Figure 1b shows the calculated emission pattern of fluorophores oriented parallel and perpendicular to the glass-water

interface, for two different axial positions ($z = 5$ nm and 200 nm). Clearly, for both orientations, more fluorescence is emitted into the glass semi-space as the fluorophores get closer to the interface. The dotted curves show the fraction of fluorescence collected by a microscope objective with $NA = 1.42$ (DF) from single molecules oriented parallel and perpendicular to the interface, as a function of the axial position. In addition, the isotropic average (DF_i) is also shown, which corresponds to the usual experimental situation of rotating fluorophores. The detected fluorescence signal from a single molecule will be proportional to the product of the excitation field and the isotropic averaged detected fluorescence. Figure 1c shows the detected fluorescence signal $F(z) = I(z)DF_i(z)$ (hereafter referred to as the exact solution) and an exponential fit. It turns out that $F(z)$ is well represented by an exponential function, just as $I(z)$, but with a steeper decay ($d_F = 87.5$ nm) and smaller background constant ($\alpha_F = 0.93$). For camera-based single molecule localization experiments it is convenient to express the fluorescence signal in terms of the number of photons detected during the acquisition time of a frame:

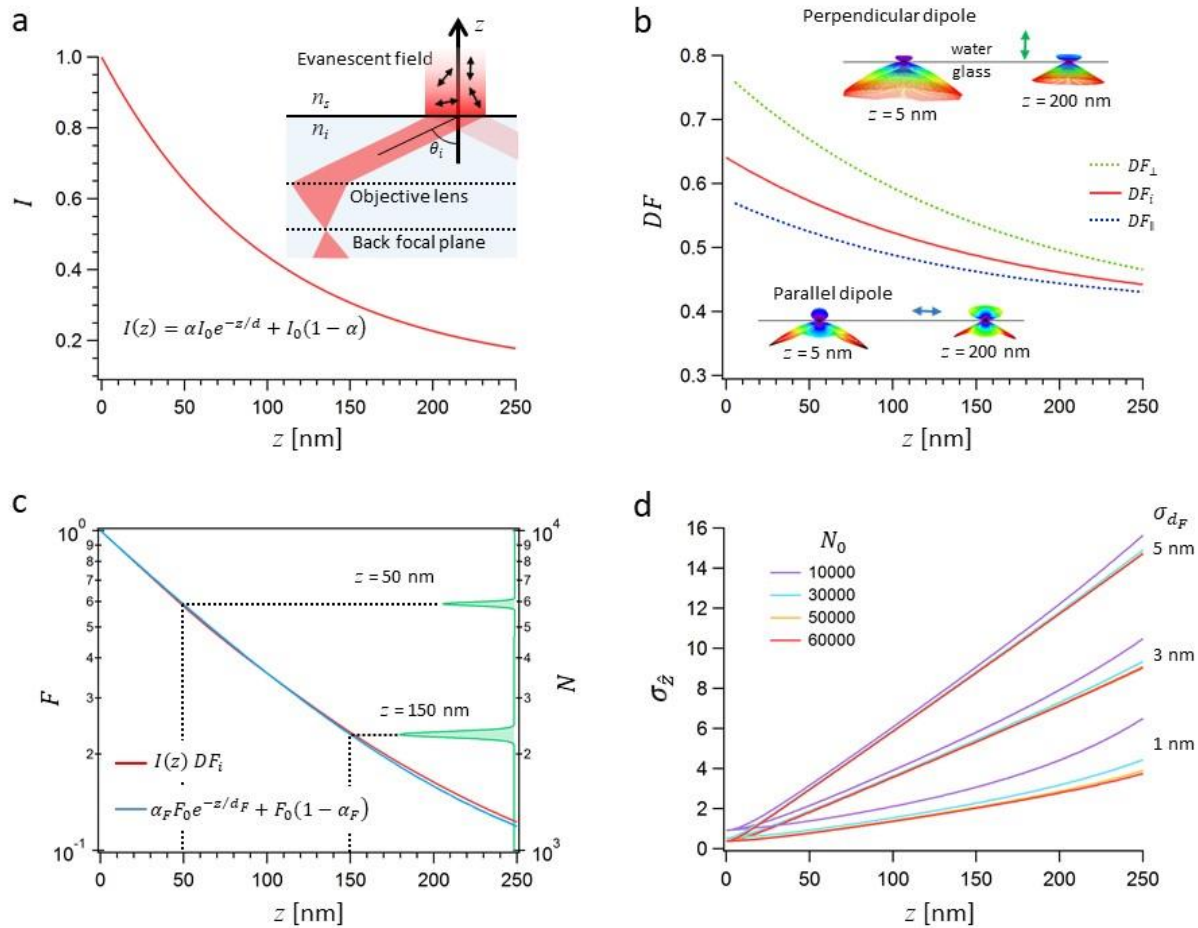$$N(z) = \alpha_F N_0\, e^{-z/d_F} + (1 - \alpha_F)N_0 \qquad (1)$$

where N_0 is the number of photons emitted by a fluorophore at $z = 0$.

Using the exponential expression of $N(z)$, an estimation of the axial position of a molecule ($\hat{z}$) can be obtained from a measurement of the number photon count emitted in a camera frame time ($\widehat{N}$), as follows:

$$\hat{z} = d_F \times ln\frac{\alpha_F N_0}{\widehat{N} - (1 - \alpha_F)N_0} \qquad (2)$$

Then, the standard error of $\hat{z}$, which ultimately determines the axial resolution, is given by:

$$\sigma_{\hat{z}} = \sqrt{\left(-\frac{d_F}{\widehat{N} - (1 - \alpha_F)N_0}\right)^2 \times \widehat{N} + \left(ln\frac{\alpha_F N_0}{\widehat{N} - (1 - \alpha_F)N_0}\right)^2 \times \sigma_{d_F}^2} \qquad (3)$$

4

Figure 1. Supercritical Illumination Microscopy by Photometric z-Localization Encoding (SIMPLE). (a) Intensity of the excitation field under TIR illumination for our experimental configuration: $\lambda_0 = 642$ nm, $n_i = 1.517$, $n_s = 1.33$ water, $\theta_i = 69.5°$, $\alpha = 0.9$. Inset: Simplified optical layout of the excitation path of a TIR fluorescence microscope. **(b)** Fraction of fluorescence signal collected by the solid angle of the microscope objective (NA= 1.42) for a fluorophore emitting at 700 nm and oriented parallel (blue dotted line) or perpendicular (green dotted line) to the glass/water interface. The solid red line represents the isotropic average of the detected fraction of emitted fluorescence, corresponding to the case of a rotating fluorophore. **(c)** Principle of SIMPLE. The axial position is retrieved from the number of emitted photons in a camera frame time either through the exact solution (solid red line) or through the exponential approximation (solid blue line) of the fluorescence signal. **(d)** Lower bound for the axial resolution of SIMPLE. Standard error of the axial position estimator for different sets of N_0 and σ_{d_F}.

5

In this expression, we have considered $\sigma_{\widehat{N}} = \sqrt{\widehat{N}}$ which arises from the fact that $\widehat{N}$ is Poisson distributed and that in typical stochastic-coordinate nanoscopy the number of emitted photons of each fluorophore is determined in one single measurement. Instead, N_0 is a reference parameter that depends on the nature of the fluorophore and the experimental conditions. Since it can be measured an arbitrary number of times, its error can be made negligible small; we have therefore considered $\sigma_{N_0} = 0$ for the computation of the theoretical lower bound for the resolution. Figure 1d shows $\sigma_{\hat{z}}$ as a function of the axial position for experimentally accessible values of N_0 and σ_{d_F}. Clearly, this method is able to deliver an axial resolution below 10 nm under usual experimental conditions. The range of sub-10 nm resolution depends strongly on the uncertainty of d_F. For $\sigma_{d_F} = 1$ nm, a resolution well below 10 nm is expected up to $z = 250$ nm for $N_0 > 10,000$. If $\sigma_{d_F} = 5$ nm, the resolution becomes fairly independent of the photon count for $N_0 > 30,000$, but the range of sub-10 nm resolution is limited to $z < 170$ nm.

It is interesting to note that up to 100 nm $N(z)$ can be approximated fairly well by a single exponential with no background ($\alpha_F = 1$). Under these conditions, and if d_F could be determined with negligible error, then $\sigma_{\hat{z}} = d_F/\sqrt{\widehat{N}}$. This bound to the resolution is analogous to the one for lateral resolution in single molecule localization, with the difference that the numerator is not the lateral size of the point-spread function, but the much smaller decay constant of the detected fluorescence signal under TIR conditions.

In practice, data is acquired and analyzed as in any other coordinate-stochastic fluorescence nanoscopy method, with the addition that the detected number of photons per frame ($\widehat{N}$) is used to determine the z-coordinate through equations (2) and (3) (Supplementary Fig. 1 and Supplementary Table 1). In order to maximize the performance of SIMPLE, an additional filtering step can be done to determine $\widehat{N}$, excluding the first and last frames of each single molecule emission event, as it is uncertain if the molecule was emitting during the complete integration time of those frames. While this post-processing step improves the quality of the 3D image, it is not determinant for the resolution achieved (Supplementary Fig. 2). N_0 can be estimated using a biological sample (*i.e.* imaging a structure whose distance to the coverslip is negligible or can be approximated by a given value) or by linking imager strands directly to the coverslip (using for example BSA-biotin/neutravidin or flat DNA-origamis). Finally, z-positions are

computed either using the exact solution or the exponential approximation (Eq. 2). The difference between the exact solution and the exponential approximation is negligible (< 1 nm) for z < 150 nm (Supplementary Figs. 3 and 4). If N_0 cannot be accurately determined, the exponential approach will be a better choice, as even a 20% error would only lead to an axial off-set shift of the image but with negligible distortions within the 0 - 200 nm axial range (Supplementary Fig. 3b and 4). Furthermore, it is worth noting that while the relative contribution of the non-evanescent field, 1-α, usually represents only a 10% of the total power at z = 0 in the commonly used objective-type TIR configurations; a misleading value in the range of 8 to 12% does not introduce distortions greater than 5 nm for $z < 150$ nm (Supplementary Figs. 3c and 4).

Figure 2 illustrates the performance of SIMPLE with 3D images of biological structures immunolabeled for DNA-PAINT. Figure 2a shows a 3D image of the β2-spectrin structure in the membrane associated periodic skeleton of dendrites and axons. The typical periodic arrangement with a period of 190 nm is clearly visible in the top view. The 3D imaging using SIMPLE allows to resolve the sub-membrane organization of β2-spectrin across the axon. A more powerful example of the axial resolution of SIMPLE are the images of microtubules shown in Figure 2b. SIMPLE is able to fully resolve the 37 nm diameter hollow circular structure of immunolabeled microtubules in COS-7 cells, with an average resolution of 8 nm (Figure 2c), an even finer level of detail than achieved with 4-Pi nanoscopy. Furthermore, imaging with this resolution in 3D makes it possible to resolve bundles of microtubules that we found to be usual in hippocampal neurons, and that would otherwise be interpreted as single microtubules (Figure 2d).
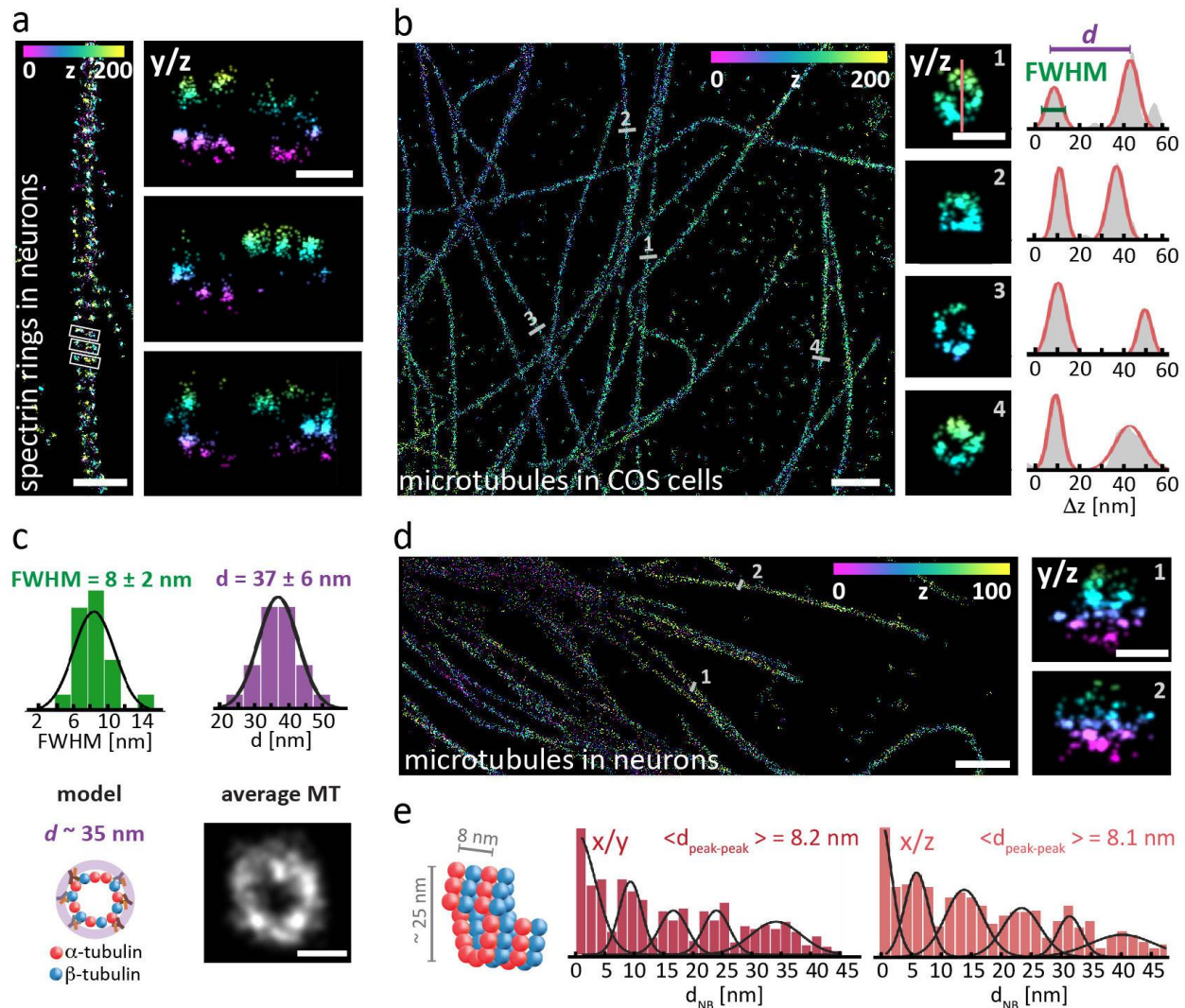
Figure 2. Cellular structures immunolabeled for DNA-PAINT super-resolved in 3D using SIMPLE. (a) β2-spectrin rings in hippocampal neurons. Left: top view (*xy*). Right: magnified side-views (*yz*) of the boxed regions in the top view. Localizations are color-coded according to their z-position. **(b)** Microtubules in COS-7 cells. Left: top view. Right: magnified side-views along the numbered lines in the top view, together with their axial profile; solid lines indicate two Gaussian fits with a distance between peaks d and half width height maximum FWHM. **(c)** Distributions of FWHM (*n* = 17) and microtubule diameters (*n* = 22). The FWHM of 8 nm with standard deviation of 2 nm demonstrates the sub-10 nm axial resolution. The experimentally determined diameter of 37 nm agrees well with the expected diameter of approximately 35 nm for immunolabeled microtubules. An average (*n* = 8) microtubule profile is also shown. **(d)** Microtubules in hippocampal neurons. Left: top view. Right: side-views along the numbered lines in the top view showing bundles of microtubules. **(e)** Schematic representation of the pseudo-helical organization of α- and β-tubulin in microtubules. Distribution of distances (*x*) of α-tubulin to first 5

8

neighbors in the transverse (*xy*) and axial (*xz*) plane of a microtubule segment of 580 nm decoded by SIMPLE. Scale bars represent 1 µm (**b** and **d**, top view); 500 nm (**a**, top view); 100 nm (**a**, side view); 50 nm (**b** and **d**, side views) and 25 nm (**c**).

Finally, we show an example of how surpassing the 10 nm resolution gives access to the supramolecular organization of structural proteins. Microtubules are a compact assembly of α- and β-tubulin organized in a pseudo-helical structure (Figure 2e). According to x-ray diffraction data, the separation distance between α-tubulin (or β-tubulin) units is of about 8 nm. The 3D resolution provided by SIMPLE and DNA-PAINT is sufficient to directly visualize this organization. However, it turns out that labelling of each individual α-tubulin is challenging due to a number of factors including steric limitations. For this reason, it was not possible to reconstruct the complete pseudo-helical organization. Still, even with incomplete labeling, the presence of an underlying structure can be interrogated for example by computing the distribution of distances to first neighbors. Figure 2d, shows the distribution of separation distances to the first five neighbors of each α-tubulin detected along 5 nm wide lines in the lateral (*xy* plane) and axial (*xz* plane) of a microtubule segment of 580 nm (Supplementary Fig. 5). The regular organization of this protein with a period of ~ 8 nm is clearly evident.

In conclusion, SIMPLE enables the location of single fluorescent molecules in the axial direction (*z*) of a microscope with sub-10 nm precision through a single measurement of the number of fluorescence photons detected in a camera frame time. Axial location is decoded taking into account the dependency on *z* of both the excitation and emission. The SIMPLE method is broadly applicable and compatible with any fluorescence nanoscopy method based on single molecule localization, and does not require any hardware modification to wide-field single molecule fluorescence microscopes. Furthermore, unlike other 3D fluorescence nanoscopy methods, the level of resolution achieved by SIMPLE is independent from the typical problem of focus drift. Using the parameters provided in Supplementary Table 1 any set of 2D data imaged under TIR illumination can be converted to 3D information. In combination with DNA-PAINT, SIMPLE delivers routinely 3D images with sub-10 nm resolution in all dimensions, giving access to the supramolecular assembly of structural proteins. Due to its simplicity and power, we believe

SIMPLE will enable a new wave of discoveries about the structure and pathways of sub-cellular structures and protein-protein interactions.

Methods

Single molecule emission

The emission pattern of single molecules was simulated as a small dipole using a Finite Difference Time Domain solver (CST Microwave Studio). The fraction of detected fluorescence was obtained by integrating the emission pattern over the solid angle of interest. We provide sets of calculations for the most usual configurations in the Supporting Information, Supplementary Table 1.

Super-resolution microscopy setup

The microscope used for TIR fluorescence SMLM was built around a commercial inverted microscope stand Olympus IX73 equipped with a high numerical aperture oil-immersion objective lens (Olympus PlanApo 60x / NA 1.42). Excitation was carried out with a circularly polarized 642 nm 1.5 W laser (MPB Communications 2RU-VFL-P-1500-642). TIR illumination was achieved with a linear translation stage (Thorlabs MT1-Z8) used to control the lateral position of the focused excitation beam on the back focal plane of the objective. The angle of incidence was set to 69.5° (maximum value allowed for our objective lens) (Supplementary Method 1 and Supplementary Fig. 6). A dichroic mirror (Semrock Di03-R 405/488/532/635-t1) and a band-pass filter (Chroma ET700/75m) were used to separate the fluorescence emission of the sample from the laser excitation. The emission light was expanded with a 2x telescope so that the pixel size of the EMCCD camera (Andor iXon3 897 DU-897D-CS0-#BV) would match the optimal value for single-molecule localization (133 nm in the focal plane). The camera and laser were controlled with custom software developed in the laboratory and described in an earlier publication[19]. Typically, we acquired sequences of 50,000-70,000 frames at 4 Hz acquisition rate with a laser power density of ~2.5 kW/cm^2.

Primary neuron culture and cell lines

Mouse (CD1) hippocampal neurons were harvested from embryonic day 17 pups, following the general guidelines of the National Institute of Health (NIH, USA) and approval of the National Department of Animal Care and Health (SENASA, Argentina), and cultured in Neurobasal medium (Gibco) supplemented with 5 mM GlutaMAX-I (Gibco) and 2% B27 supplement (Gibco) at 37 °C and 5% CO_2. Neurons were seeded at a density of 125 cells/mm^2 on #1.5 thickness glass-bottomed chamber slides (Lab-Tek II, Thermo Fisher Scientific) and incubated for either 3 or 28 days, respectively. To increase cell attachment, glass slides were previously coated with 0,05 mg/mL poly-L-lysine (overnight at 37°C) (Sigma Aldrich) and 1 μg/μL Laminin (3 h at 37°C) (Sigma Aldrich).

Culture of COS-7 cell lines were grown in Dulbecco's modified Eagle's medium (DMEM) supplemented with 10% fetal calf serum, penicillin (100 units/ml), streptomycin (100 μg/ml) and 2 mM L-glutamine (Gibco) at 37 °C and 5% CO_2.

Sample preparation and imaging

Neurons and COS-7 cells were fixed and permeabilized in PHEM buffer (60 mM PIPES, 25 mM HEPES, 5 mM EGTA, 1 mM $MgCl_2$, pH=7.0), supplemented with 0.25% glutaraldehyde, 3.7% paraformaldehyde, 3.7% sucrose and 0.1% Triton X-100, for 20 min at room temperature. Auto-fluorescence was quenched by incubating the samples in 0.1 M glycine in PBS for 15 minutes followed by 3× washes with PBS. The fixed and quenched samples were blocked with 5% BSA in PBS containing 0.01% Triton X-100 for 1 h. Spectrin in neurons (Fig. 2a) was labeled with a mouse monoclonal primary antibody anti-β-Spectrin II (Clone 42/B-Spectrin II, BD Biosciences) for 1 h at room temperature using a 1:400 dilution in 5% BSA in PBS, followed by 3× washes with PBS. DNA-conjugated secondary antibody staining was performed by incubating the sample with a donkey anti-mouse secondary fragment antibody (Jackson ImmunoResearch, 715-007-003) at a 1:100 dilution in 5% BSA in PBS for 1 h at room temperature, followed by 3× washes with PBS. Microtubules in COS-7 cells (Fig. 2b) and in neurons (Fig. 2d) were treated with anti α-tubulin and anti β-tubulin primary antibodies for 1 h at room temperature using 1:400 dilutions in 5% BSA in PBS, followed by 3× washes with PBS (mouse monoclonal anti-α-Tubulin, clone TUB-A4A Sigma

11

Aldrich; mouse monoclonal tyrosine anti-α-Tubulin, clone TUB-1A2 Sigma Aldrich; rabbit polyclonal anti-β-III-Tubulin, Abcam #ab 18207 for neurons; and rabbit polyclonal anti-β-II-Tubulin Abcam #ab 196 for COS-7 cells, kind gift of Dr. Jesus Avila, Centro de Biologia Molecular "Severo Ochoa" CBMSO, Consejo Superior de Investigaciones, Cientificas, Universidad Autonoma de MadridUAM, C/ Nicolas Cabrera, 1. Campus de Cantoblanco, 28049 Madrid, Spain[20]). In both cases secondary staining was done with a mix of DNA-conjugated donkey anti-mouse fragment antibody (Jackson ImmunoResearch, 715-007-003) and donkey anti-rabbit DNA-conjugated secondary fragment antibody (Jackson ImmunoResearch, 711-007-003) was used at a 1:100 dilution in 5% BSA in PBS for 1 h at room temperature, followed by 3x washes with PBS.

For exclusive α-tubulin imaging (Fig. 2e), neurons were treated with anti α-tubulin primary antibody (mouse monoclonal tyrosine anti-α-Tubulin, clone TUB-1A2, Sigma Aldrich) and the donkey anti-mouse DNA-conjugated secondary fragment antibody (Jackson ImmunoResearch, 715-007-003), under the same experimental conditions described above.

Antibody conjugation to DNA-PAINT docking sites (5'-TATGTAACTTT-3'-Thiol and 5'-ATTACTTCTTT-3'-Thiol, biomers.net GmbH, for the donkey anti-mouse and the donkey anti-rabbit conjugates respectively) was performed using maleimidePEG2-succinimidyl ester coupling reaction according to a published protocol[2] as described in Supplementary Method 2.

100 nm gold nanoparticles (BBI solutions) were added as fiducial markers for drift correction by incubating the sample for 5 min in a 1:2 solution of nanoparticles in PBS. After 3× washes with PBS, PAINT buffer (Buffer B+: 5 mM Tris-HCl, 10 mM $MgCl_2$, 1 mM EDTA and 0.05 % Tween 20 at pH 8.0) containing fluorescently labeled DNA imager strands (Img1: ATTO655-5'-AGTTACATAC-3' and Img2: ATTO655-5'-AGAAGTAATG-3', biomers.net GmbH, for imaging anti-mouse and anti-rabbit DNA-conjugated secondary antibodies respectively) was added to the sample. Imager strands concentrations were 20 nM Img1 for spectrin imaging (Fig. 2a), 120 pM Img1 for α-tubulin imaging (Fig. 2e) and 80 pM Img1 + 80 pM Img2 for α-tubulin + β-tubulin imaging (Fig. 2b and d). Samples were then used immediately for DNA-PAINT imaging.

Data acquisition, analysis and 3D image rendering

Lateral *(x,y)* molecular coordinates and photon counts ($\widehat{N}$) were obtained using the Localize module of Picasso software[2], selecting a threshold net gradient of 3000 for microtubules, and 1000 for spectrin rings, and enabling the symmetric PSF fitting method. To accurately calculate the photon-counts of the localizations, we input the specific noise statistics parameters of the EM-CCD camera. Drift correction was carried out with a combination of redundant cross-correlation and fiducial markers approach using the Render module of Picasso. Photon-counts were corrected using the illumination profile of the beam (measured by imaging a 1 μM Alexa Fluor 647 solution with the same incident angle as in the biological experiments). Next, localizations were filtered to discard the frames corresponding to the switching (ON or OFF) of the fluorophores during the frame acquisition, whose photon count would be lower and lead to falsely high *z* coordinates. To ensure the molecule was emitting during the whole exposure time, localizations were kept as valid only in the case that other localizations, reasonably attributed to the same fluorophore (within a 20 nm distance), were detected in the previous and subsequent frames (Supplementary Figs. 1 and 2). Molecules detected for less than three frames were thus ignored.

For each image, a photon count was assigned to $z = 0$ (N_0). We set it using biological considerations (*i.e.* the estimated distance of a structure to the cover-glass). For example, spectrin rings are attached to the plasma membrane, hence we set N_0 so that the lower bound of the rings sit at z = 5 - 10 nm from the coverslip (Fig. 2a; Supplementary Figs. 2 and 4). A similar approach was used to set N_0 for microtubules images (Fig. 2b and 2d; Supplementary Figs. 4 and 5). Alternatively, a membrane marker or a flat DNA-origami labelled with a different imager strand could be used to estimate N_0, with limited influence on the image quality and precision (Supplementary Fig. 3b and 4). For each localization, *z*-localization precision (σ_z) could be calculated from Eq. (3) using a σ_d value of 1 nm, based on an error of 0.5° in the determination of the incident angle.

Finally, z-color-coded image rendering was done using the ImageJ plug-in ThunderStorm[21], importing the list of *(x, y, z)*. A Gaussian filter with σ = 2 nm was used for all three dimensions. A lenient density filter was applied, to discard localizations with less than 100 neighbours in a 67nm

radius, to enhance contrast by suppressing some of the non-specific localizations of the background.

α-tubulin structure analysis

The 5-first neighbours' distance analysis for α-tubulin was made as follows. First, the list of (x, y) coordinates was multiplied by a rotation matrix, in order to align the microtubule with the x- axis. Once rotated, scatter plots of x/y and x/z localizations were built and two extreme values for z and y were selected, in order to define an upper and a lower region of the microtubule in the x/z plane and two lateral extreme regions in the x/y plane. Next, line profiles located along the x-direction with a width of 5 nm were obtained for both plots in their extreme regions (four line profiles overall). The separation distances between each localization detected along these lines and the nearest five neighbours were measured. Data corresponding to opposite line profiles from the same image were grouped together, giving rise to the histograms shown in Fig. 2e.

Data availability.

The data sets generated and analyzed in this study are available from the corresponding author upon reasonable request.

Acknowledgements

Author contributions

S.S. and F.D.S. conceived the approach and wrote the manuscript with input from all authors. A.M.S., B.S., S.S. and F.D.S. developed the analysis method. A.M.S. and B.S. acquired and analyzed the data. D.J.W. helped with the data analysis. A.M.S. and S.S. produced the custom-made DNA-PAINT antibodies. J.L, R.B, N.U., D.R. and A.O.C. contributed the primary neuron cultures and COS-7 cell lines, and carried out the spectrin and microtubules immunostaining with the custom-made DNA-PAINT antibodies. F.D.S., M.P-P and G.A. simulated the emission pattern of single molecules. D.M.O. discussed results and commented on the manuscript.

Competing interests

The authors declare no competing interests.

References

1. Jungmann, R. *et al.* Single-molecule kinetics and super-resolution microscopy by fluorescence imaging of transient binding on DNA origami. *Nano Lett.* **10**, 4756–4761 (2010).

2. Schnitzbauer, J., Strauss, M. T., Schlichthaerle, T., Schueder, F. & Jungmann, R. Super-resolution microscopy with DNA-PAINT. *Nat. Protoc.* **12**, 1198–1228 (2017).

3. Balzarotti, F. *et al.* Nanometer resolution imaging and tracking of fluorescent molecules with minimal photon fluxes. *Science (80-.).* **355**, 606–612 (2017).

4. Sahl, S. J., Hell, S. W. & Jakobs, S. Fluorescence nanoscopy in cell biology. *Nat. Rev. Mol. Cell Biol.* **18**, 685–701 (2017).

5. Li, Y. *et al.* Real-time 3D single-molecule localization using experimental point spread functions. *Nat. Methods* **15**, 367–369 (2018).

6. Bourg, N. *et al.* Direct optical nanoscopy with axially localized detection. *Nat. Photonics* **9**, 587–593 (2015).

7. Franke, C., Sauer, M. & van de Linde, S. Photometry unlocks 3D information from 2D localization microscopy data. *Nat. Methods* **14**, 41–44 (2017).

8. Hell, S. W. & Stelzer, E. H. K. Properties of a 4Pi confocal fluorescence microscope. *J. Opt.*

15

Soc. Am. A **9**, 2159 (1992).

9.   Schmidt, R. *et al.* Spherical nanosized focal spot unravels the interior of cells. *Nat. Methods* **5**, 539–44 (2008).

10.   Curdt, F. *et al.* isoSTED nanoscopy with intrinsic beam alignment. *Opt. Express* **23**, 30891 (2015).

11.   Shtengel, G. *et al.* Interferometric fluorescent super-resolution microscopy resolves 3D cellular ultrastructure. *Proc. Natl. Acad. Sci. U. S. A.* **106**, 3125–3130 (2009).

12.   Aquino, D. *et al.* Two-color nanoscopy of three-dimensional volumes by 4Pi detection of stochastically switched fluorophores. *Nat. Methods* **8**, 353–359 (2011).

13.   Huang, F. *et al.* Ultra-High Resolution 3D Imaging of Whole Cells. *Cell* **166**, 1028–1040 (2016).

14.   Chizhik, A. I., Rother, J., Gregor, I., Janshoff, A. & Enderlein, J. Metal-induced energy transfer for live cell nanoscopy. *Nat. Photonics* **8**, 124–127 (2014).

15.   Kaminska, I. *et al.* Distance Dependence of Single-Molecule Energy Transfer to Graphene Measured with DNA Origami Nanopositioners. *Nano Lett.* **Just accep**, acs.nanolett.9b00172 (2019).

16.   Karedla, N. *et al.* Three-dimensional single-molecule localization with nanometer accuracy using Metal-Induced Energy Transfer (MIET) imaging. *J. Chem. Phys.* **148**, 204201 (2018).

17.   Mattheyses, A. L. & Axelrod, D. Direct measurement of the evanescent field profile produced by objective-based total internal reflection fluorescence. *J. Biomed. Opt.* **11**, 014006 (2006).

18.   Axelrod, D. & Hellen, E. H. Emission of Fluorescence at an Interface. *Methods Cell Biol.* **30**, 399–416 (1989).

19.   Barabas, F. M., Masullo, L. A. & Stefani, F. D. Tormenta : An open source Python-powered control software for camera based optical microscopy. *Rev. Sci. Instrum.* **87**, 126103 (2016).

20.   Armas-Portela, R., Parrales, M. A., Albar, J. P., Martinez-A., C. & Avila, J. Distribution and characteristics of βII tubulin-enriched microtubules in interphase cells. *Exp. Cell Res.*

(1999). doi:10.1006/excr.1999.4426

21. Ovesný, M., Křížek, P., Borkovec, J., Švindrych, Z. & Hagen, G. M. ThunderSTORM: a comprehensive ImageJ plug-in for PALM and STORM data analysis and super-resolution imaging. *Bioinformatics* **30**, 2389–2390 (2014).

Supplementary Information

Three-dimensional total internal reflection fluorescence nanoscopy with sub-10 nm resolution

Alan M. Szalai, Bruno Siarry, Jerónimo Lukin, David J. Williamson, Nicolás Unsain, Raquel Becerra, Damián Refojo, Alfredo Cáceres, Mauricio Pilo-Pais, Guillermo Acuna, Dylan M. Owen, Sabrina Simoncelli and Fernando D. Stefani
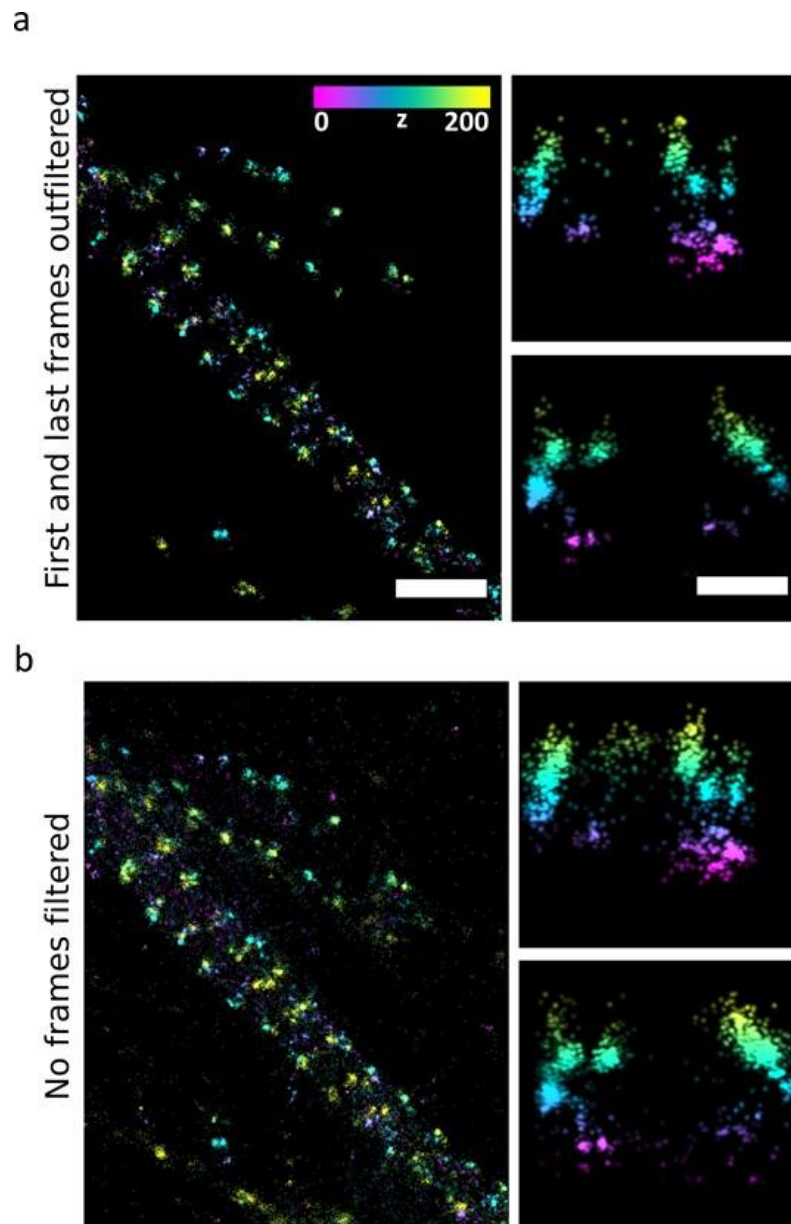
Supplementary Figure 1	Data analysis and z assessment.
Supplementary Figure 2	Influence of the first and last frame filtering step on image quality.
Supplementary Figure 3	Quantification of the differences in z values obtained using the exact solution of the fluorescence signal or the exponential approximation, for varying ⍰ and N_0.
Supplementary Figure 4	Comparison of side-view reconstructions by SIMPLE using different computation methods.
Supplementary Figure 5	x/y and x/z images of a single microtubule immunolabeled with α-tubulin.
Supplementary Figure 6	Calibration of the TIRF excitation angle.
Supplementary Table 1	Axial dependence of the collected fluorescence signal.
Supplementary Method 1	TIRF angle calibration
Supplementary Method 2	DNA-antibody coupling reaction

Supplementary Figures
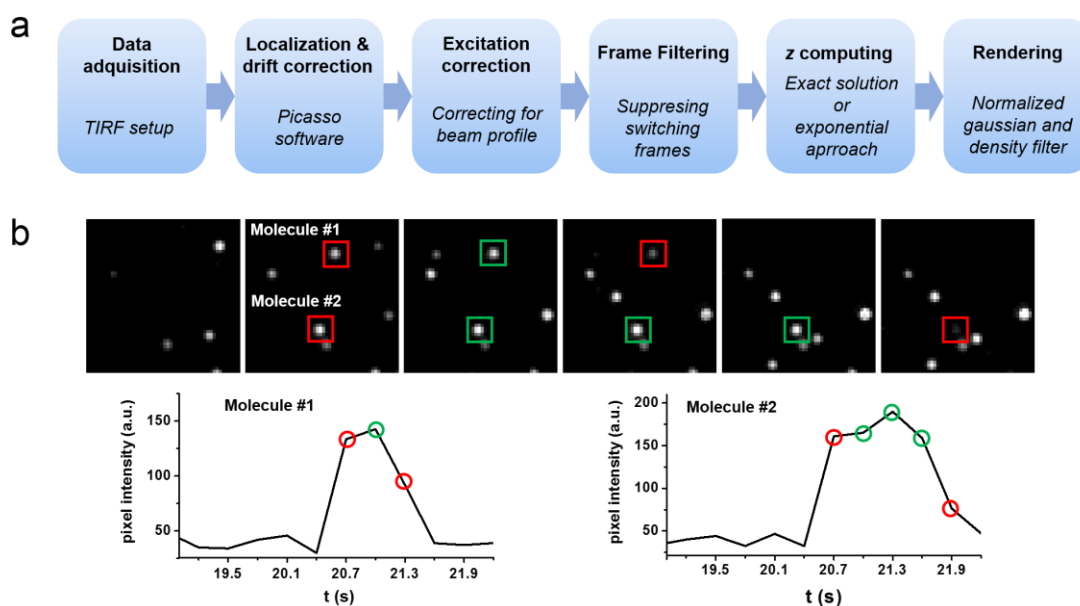
Supplementary Figure 1. Data analysis and *z* assessment. (**a**) Workflow of the post-processing step (detailed in Methods). Single molecules are detected and localized using any single molecule localization microscopy software (in our case, Picasso).[1] In this step, drift correction using autocorrelation or both autocorrelation and fiducials markers is carried out. Next, if the excitation is spatially inhomogeneous (*i.e.* due to Gaussian shape of the excitation beam), the number of photons of each localization within the region of interest has to be corrected to take it into account. Next, a frame filtering step can be performed to use of localizations that lasted at least three frames, and compute the photon count excluding potentially misleading first and last frames. Then, the *z* position of each detected molecule is estimated from the photon count either numerically using the exact solution of the fluorescence signal, or using the exponential approach (equation 2). Finally, the 3D super-resolved image is rendered with appropriate software (we used the ImageJ plug-in ThunderStorm)[2]. (**b**) Camera frames sequence and examples of local time traces of two single molecules. The red squares and circles indicate first and last frames that are dismissed during the optional frame filtering step because it cannot be assured that those molecule were emitting during the whole frame duration. Computing those

frames could lead to a photon count lower than expected. The effect of this frame filtering is

illustrated in Supplementary Fig. 2.

Supplementary Figure 2. Influence of the first and last frame filtering step on image quality. Overview image of β2-spectrin rings in neurons and magnified side-view reconstructions, *i.e. z–y* projections, of the boxed regions in the *x–y* view where the rendering was done with (**a**) and without (**b**) the frame filtering step of the localizations (described in Methods and Supplementary Fig. 1). In the *x–y* view, the filter's action resembles the one of a density filter, improving contrast by suppressing isolated or unspecific events. In the *z–y* projections, we see that the filter

suppresses localizations that are wrongly assigned with higher z coordinate due to the incorrectly

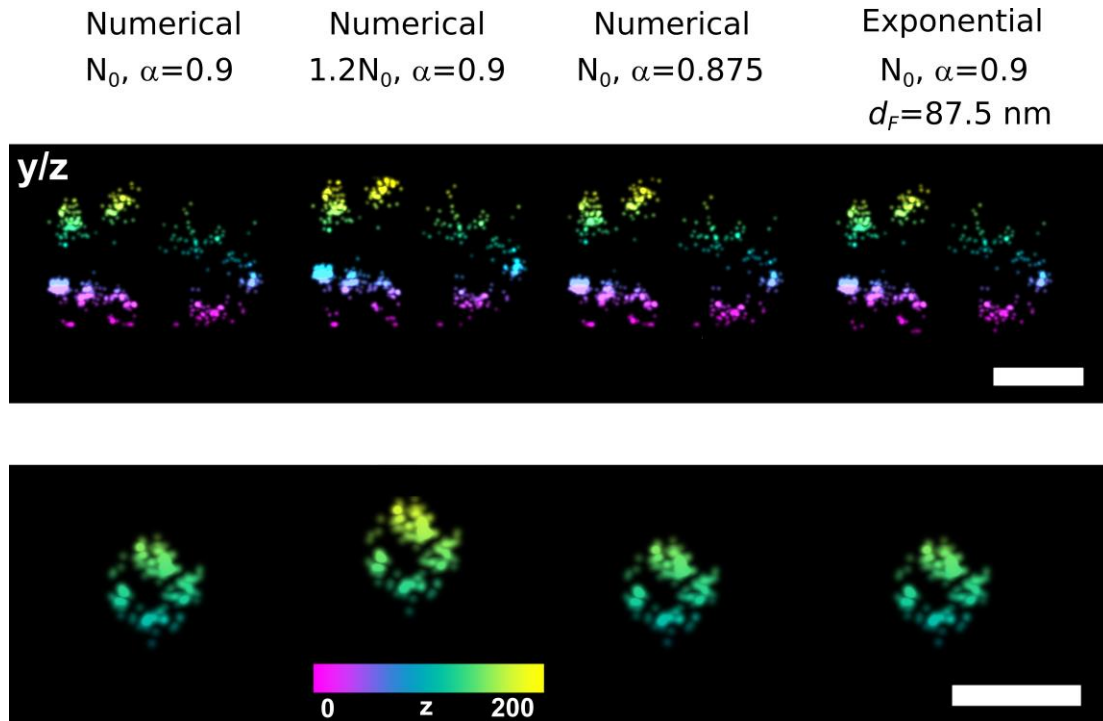determined lower photon count. Scale bars represent 1 μm (top view) and 100 nm (side view).
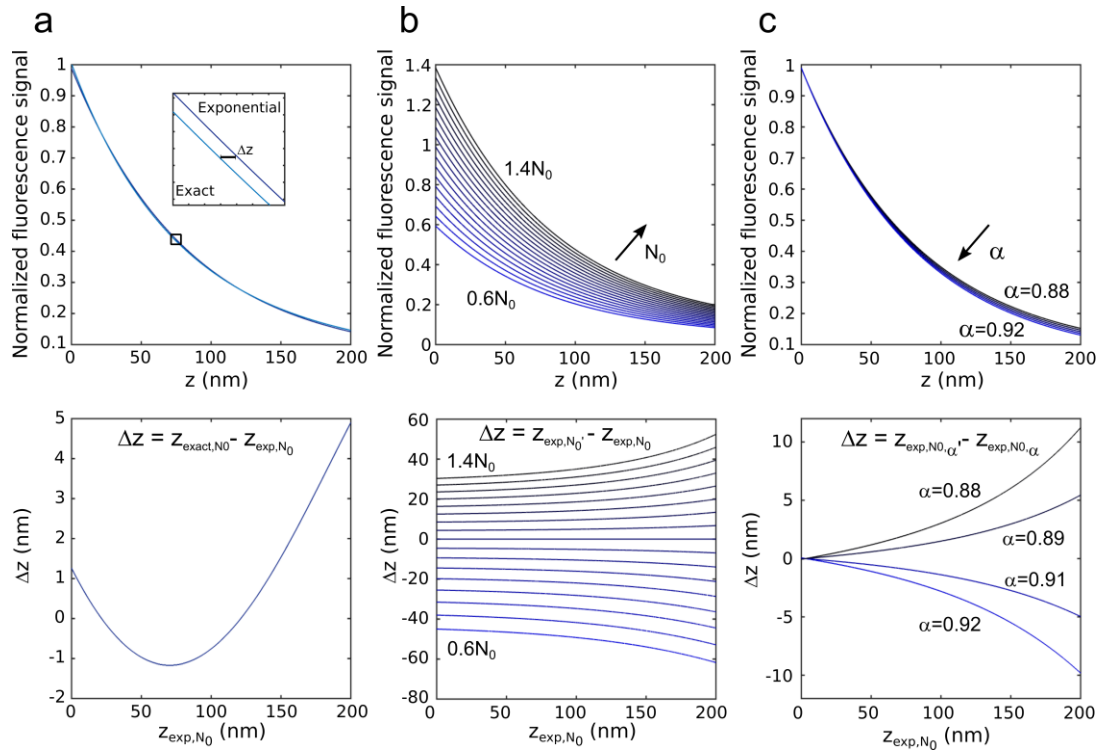
Supplementary Figure 3. Quantification of the differences in z values obtained using the exact solution of the fluorescence signal or the exponential approximation, for varying ▢ and N_0. (a) Exact solution vs. exponential approximation. Top: Exact solution and exponential approximation of the detected fluorescence signal as a function of z. The inset shows the shift Δz between the curves for the range of z from 71 to 78 nm. Bottom: Δz as a function of z from the exponential curve (z_{exp,N_0}). For $z < 200$ nm, the exponential calculation gives an error in z below 6 nm. In the range of 0-150 nm, the difference in z positions calculated using either of both methods is negligible (<1 nm). **(b)** Influence of N_0. Top: Detected fluorescence signal (exponential approx.) for N_0 varying from -40% to +40%. Bottom: Δz as a function of z_{exp,N_0}. Remarkably, a wrong determination of N_0 by 40% mainly introduces an axial off-set, with < 9 nm distortions up to $z = 150$ nm. If N_0 is determined with a precision better than 20%, the < 9 nm distorted region extends to 200 nm. It is also noteworthy that negative axial shifts achieved when N_0 is underestimated do not modify z-distances under the exponential approach (Δz remains negative and constant), because the equation used to compute z allows negative positions for bright events by extrapolation. Oppositely, the numerical estimation z using the exact solution only

allows positive axial positions. Consequently, an accurate choice of N_0 turns more critical when the numerical estimator is used. In other words, although the exponential approximation introduces a known shift (**a**), it is more robust to uncertainty or variations of N_0. (**c**) Influence of α. Top: exponential approximation of the detected fluorescence as a function of z for α in the range of 0.88 to 0.92. This limits correspond to a non-evanescent component of the illumination field 12% and 8% of the total power at $z = 0$, instead of 10% as in our experimental configuration. Variations of α in this range do not introduce distortions greater than 5 nm for $z < 150$ nm.

Numerical	Numerical	Numerical	Exponential
N_0, $\alpha=0.9$	$1.2N_0$, $\alpha=0.9$	N_0, $\alpha=0.875$	N_0, $\alpha=0.9$
			$d_F=87.5$ nm

Supplementary Figure 4. Comparison of side-view reconstructions by SIMPLE using different computation methods. Side views (*i.e. z-y* projections) of a spectrin ring (top) and a microtubule (bottom) obtained with different z -computation approaches. In the first images (left), z was computed numerically using the exact solution using $\alpha = 0.90$ and $N_0 = 50.000$. The second images shows the influence of choosing another N_0 ($1.2N_0$). We can see that the choice of N_0 mainly acts as an offset to the z-coordinate, influencing principally on the measured distance to the cover-slide. The third column shows the profiles calculated with a different α value. Finally, the side-view reconstructions achieved with the exponential approach ($d_F = 87.5$ nm) are shown in the last column. No significant axial distortions are observed over this range of parameters. Scale bars represent 100 nm.
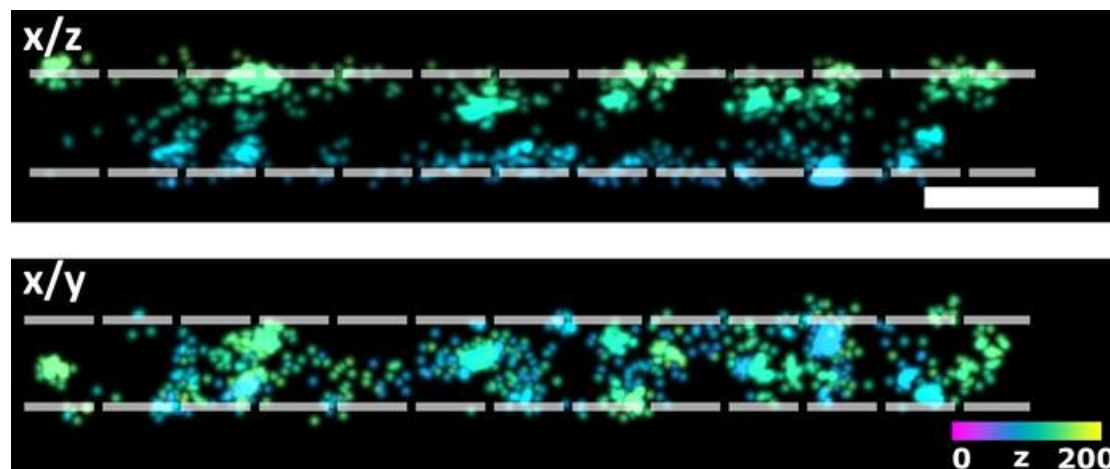
Supplementary Figure 5. *x/y* **and** *x/z* **images of a single microtubule immunolabeled with** α-**tubulin.** The dotted line represents the 5 nm-width regions where the first five neighbors' analysis was carried out. The scale bar represents 100 nm.
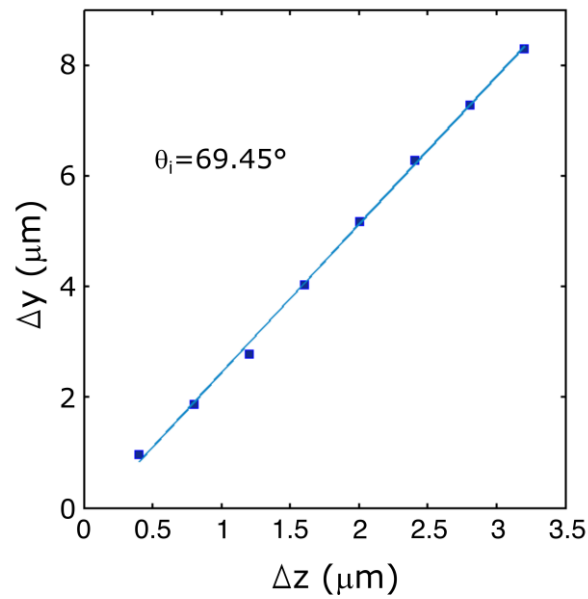
Supplementary Figure 6. Calibration of the TIRF excitation angle. Displacement of the excitation laser beam center Δy versus the axial position of the sample Δz (according to Supplementary Method 1). Linear fitting allows determination of θ_i = 69.45º, in line to the specified limit of our objective (69.5º for an Olympus PlanApo 60x / NA 1.42).

Supplementary Tables

z [nm]		λ = 500 nm					λ = 530			
	NA	1.4	1.42	1.45	1.49		1.4	1.42	1.45	1.49
5		0.593	0.628	0.680	0.727		0.593	0.628	0.681	0.728
50		0.531	0.550	0.577	0.600		0.534	0.554	0.583	0.606
100		0.486	0.497	0.510	0.519		0.491	0.502	0.516	0.527
150		0.454	0.460	0.466	0.470		0.459	0.465	0.473	0.477
200		0.432	0.435	0.438	0.440		0.437	0.440	0.444	0.446
250		0.417	0.418	0.420	0.421		0.421	0.423	0.425	0.426
300		0.409	0.410	0.410	0.411		0.412	0.413	0.414	0.415
350		0.403	0.403	0.403	0.403		0.403	0.403	0.404	0.404
400		0.394	0.394	0.394	0.395		0.396	0.397	0.397	0.397
450		0.391	0.391	0.391	0.391		0.393	0.394	0.394	0.394
500		0.389	0.389	0.389	0.389		0.392	0.392	0.392	0.392

z [nm]		λ = 560					λ = 590			
	NA	1.4	1.42	1.45	1.49		1.4	1.42	1.45	1.49
5		0.593	0.629	0.682	0.729		0.594	0.630	0.683	0.730
50		0.537	0.558	0.588	0.612		0.540	0.562	0.593	0.618
100		0.495	0.507	0.523	0.535		0.499	0.512	0.529	0.542
150		0.464	0.471	0.479	0.485		0.469	0.476	0.485	0.492
200		0.441	0.445	0.450	0.452		0.446	0.450	0.455	0.458
250		0.425	0.427	0.429	0.431		0.429	0.431	0.434	0.436
300		0.416	0.417	0.418	0.419		0.419	0.421	0.422	0.423
350		0.406	0.407	0.407	0.407		0.410	0.410	0.411	0.412
400		0.400	0.400	0.400	0.401		0.402	0.403	0.403	0.403
450		0.396	0.396	0.396	0.396		0.398	0.398	0.398	0.399
500		0.391	0.392	0.392	0.392		0.394	0.394	0.394	0.394

z [nm]		λ = 620					λ = 670			
	NA	1.4	1.42	1.45	1.49		1.4	1.42	1.45	1.49
5		0.594	0.630	0.684	0.731		0.594	0.630	0.684	0.732
50		0.543	0.565	0.597	0.624		0.546	0.570	0.603	0.631
100		0.503	0.517	0.535	0.549		0.509	0.524	0.543	0.559
150		0.473	0.481	0.491	0.498		0.479	0.488	0.500	0.508
200		0.450	0.455	0.460	0.464		0.456	0.462	0.469	0.473
250		0.433	0.436	0.439	0.441		0.439	0.442	0.446	0.449
300		0.423	0.425	0.426	0.427		0.428	0.431	0.433	0.434
350		0.413	0.414	0.415	0.415		0.418	0.419	0.420	0.421
400		0.405	0.406	0.407	0.407		0.409	0.410	0.411	0.412
450		0.401	0.401	0.401	0.402		0.406	0.406	0.407	0.407
500		0.396	0.396	0.396	0.397		0.400	0.400	0.400	0.401

z [nm]		λ = 700					λ = 720			
	NA	1.4	1.42	1.45	1.49		1.4	1.42	1.45	1.49
5		0.598	0.634	0.688	0.735		0.593	0.630	0.684	0.732
50		0.546	0.570	0.604	0.632		0.549	0.574	0.609	0.638
100		0.509	0.524	0.544	0.560		0.514	0.530	0.552	0.569
150		0.479	0.488	0.500	0.509		0.485	0.495	0.509	0.518
200		0.456	0.462	0.469	0.474		0.463	0.469	0.478	0.483
250		0.438	0.442	0.446	0.449		0.445	0.449	0.454	0.458
300		0.428	0.430	0.433	0.434		0.434	0.437	0.440	0.442
350		0.417	0.418	0.420	0.421		0.423	0.425	0.427	0.428
400		0.409	0.410	0.411	0.411		0.414	0.416	0.417	0.417
450		0.405	0.405	0.406	0.406		0.410	0.411	0.411	0.412
500		0.402	0.402	0.403	0.403		0.404	0.404	0.405	0.405

Supplementary Table 1. Axial dependence of the collected fluorescence signal. Values of DF_i as a function of z for various values of wavelength (λ) and numerical aperture (NA), which together with the axial dependence of the illumination field allow users to extract the decay (d_F) and the background constant (α_F). Alternatively, users can directly obtain d_F and α_F by simply input of their experimental parameters in the supplemented MATLAB script (Supplementary Software 1).

Supplementary Methods

Supplementary Method 1: TIRF angle calibration

Incident angle of the excitation beam was determined as previously described.[3] Briefly, 1 µM AlexaFluor 647 solution was illuminated with an incident angle $\theta_i > \theta_c$ and the sample was translated in z-direction from z = 0 to z = 10 µm, in 0.4 µm steps (Prior ProScan III). As a consequence of the z-translation of the sample the excitation spot was displaced in a lateral direction (y). The value of θ_i was obtained by fitting the dependence of lateral movement of the center of the excitation beam on the z-translation with a linear regression, where $\Delta y = m\Delta z + c$ and arctan(m) = θ_i (See calibration data and fit in Supplementary Fig. 6).

Supplementary Method 2: DNA-antibody coupling reaction

DNA labelling of a fragment secondary antibody (donkey anti-mouse IgM, 715-007-003 or donkey anti-rabbit IgM, 711-007-003, Jackson ImmunoResearch) was performed using the maleimidePEG2-succinimidyl ester coupling reaction.[4] In order to reduce the thiolated DNA for the maleimide reaction, 15 µL of 1 mM thiol-DNA (5'-TATGTAACTTT-3'-Thiol and 5'-ATTACTTCTTT-3'-Thiol, biomers.net GmbH, for the donkey anti-mouse and the donkey anti-rabbit conjugates respectively) were incubated with 35 µL of 250 mM DDT (Thermo Fisher Scientific) freshly prepared solution (1.5 mM EDTA, 0.5x PBS, pH 7.2) on a shaker, in the dark, for 2 h at room temperature. 30 min after the reduction of the thiol-DNA started, 30 µL of 26 µM fragment antibody was incubated with 0.7 µL of 23.5 mM Maleimide-PEG2-succinimidyl ester (Sigma-Aldrich) solution on a shaker, in the dark, for 90 min at 4ºC. Prior DNA-antibody conjugation, both sets of reactions were purified using an illustra MicroSpin G-25 column (GE Healthcare) to remove excess of DDT and a Zeba desalting column (Thermo Fisher Scientific) to remove excess of cross-linker. Next, both flow-through of the columns were mixed and incubated on a shaker, in the dark, overnight at 4ºC. The next day, DNA excess was removed by Amicon spin filtration (30 kDa). Antibody-DNA concentration was measure with the

30

NanoDrop spectrophotometer and adjusted to 14 μM with PBS. DNA-labelled antibodies were store for a maximum of 6 months at 4 °C.

Supplementary References

1. Schnitzbauer, J., Strauss, M. T., Schlichthaerle, T., Schueder, F. & Jungmann, R. *Nat. Protoc.* **12**, 1198–1228 (2017).

2. Ovesný, M., Křížek, P., Borkovec, J., Švindrych, Z. & Hagen, G. M. *Bioinformatics* **30**, 2389–2390 (2014).

3. Niederauer, C. *et al*. *Opt. Express* **26**, 20492-20506 (2018).

4. Jungmann, R. *et al*. *Nat. Methods* **11**, 313–8 (2014).